RSC Advances

ROYAL SOCIETY OF CHEMISTRY

www.rsc.org/advances

RSC Advances

PAPER

Received 00th May 2015,
Accepted 00th May 2015
DOI: 10.1039/x0xx00000x

www.rsc.org/

Nickel doped nanohydroxyapatite : Vascular endothelial growth factor inducing biomaterials for bone tissue engineering

Anu Priya B.[a], Senthilguru K. [a], Agarwal T. [a], Gautham Hari Narayana S.N. [a], Giri S. [b], Pramanik K. [a], Pal K. [a], Banerjee I. [a] *

Biomaterial induced activation of vascular endothelial growth factor (VEGF) pathway for angiogenesis has now gaining recognition as an effective option for tissue engineering. In this context, bivalent nickel (Ni^{+2}) ion doped nano-hydroxyapatites (nHAp) were synthesized by wet chemical method, characterized and evaluated for their osteoconductive and proangiogenic properties. Electron microscopy (FESEM and TEM) along with ICP-OES analysis ensured formation of Ni^{+2} doped nanoparticles (average ferret diameter 15-17 nm). The 'apatite identity' of the nanoparticles was confirmed by XRD and FT-IR. Analysis revealed that Ni^{+2} doping caused no significant distortion in the crystal structure but decreased the crystalinity of nHAp considerably. Similarly no major variation in the surface area (BET analysis), the zeta potential and the protein absorption was observed among the samples. Biological characterization showed that Ni^{+2} doping influenced the cell viability, proliferation and differentiation of bone cells (MG-63) in a concentration dependent way. ELISA and RT-PCR study revealed that Ni^{+2} doped nHAp induced cellular VEGF expression many fold in comparison to control. Profiling of hypoxia inducible factor 1 alpha (HIF-1α) expression by immuno-cytochemistry and RT-PCR implied its involvement in cellular VEGF production. In conclusion, Ni^{+2} doped nHAp may serve as proangiogenic-osteogenic biomaterial for bone tissue engineering.

1. Introduction:

One of the major challenges associated with the clinical translation of scaffold-based bone tissue engineering is to ensure vascularization after implantation in vivo. Vascularization is essential for the transport of the nutrients and gases to the cells present at the distal location of an implanted scaffold which can hardly be reached through interstitial fluid diffusion (diffusion transport limit is 200 µm approx.) [1-2]. An inadequate vascularization often hinders the formation of the regenerative callus resulting in atrophic non-union of the bone. During last couple of years, numerous strategies have been implemented to promote vascularization of bone tissue constructs. These include the use of angiogenic growth factors (VEGF, PDGF) to induce endothelial cell proliferation and migration [3-4], direct application of endothelial or its progenitor cell [5], development of microfluidic based network inside the scaffold (analogues to natural vascularization) [6], and the activation of the genetic-network of the cells for enhanced production of angiogenic growth factors. The short half-life, high cost and uncontrolled 3D distribution in vivo limits the application of angiogenic growth factors in the bone tissue engineering. The cell-based approach of promoting angiogenesis failed to meet the expectation for a number of reasons. Firstly, a great phenotypic variation exists among endothelial cells (depending on the source, organ and tissue location) which profoundly influence the angiogenic potential, molecular permeability, homeostasis, vascular tone and even immune tolerance. Secondly, a successful synthesis of vasculature needs a controlled co-culture of a number of cells along with the endothelial cells, which is difficult to achieve [7]. The strategies pertaining to the development of microfluidic network based vasculature analogue involves sophisticated and costly infrastructure which limit its translation. Among the aforesaid vascularization strategies, gene therapy is probably the most cost-effective method. However, the difficulty lies in targeting specific host cells and the risk of introduction of vector gene into the patient [8-9].

Recently, research has been focussed on biomaterials that are capable of stimulating the cells for biased production of angiogenic factors in vivo. In this regard, a common approach is to create a tissue hypoxia condition in vivo. It is already known that angiogenesis get induced by hypoxic condition through HIF-1α (Hypoxia inducible factor-1α) pathway. Moreover, hypoxia couples angiogenesis to osteogenesis [10]. HIF-1α is a transcription factor, responsible for activation of VEGF gene which in turn produces VEGF, a potential mitogen for endothelial cells. Under normoxic condition, prolyl hydroxylase (PH) induces ubiquitin mediated proteosomal degradation of HIF-1α [11]. In the absence of oxygen, PH fails to degrade HIF-1α leading to an increase in VEGF production. It is important to mention that metal ions including cobalt (Co^{+2}), copper (Cu^{+2}), chromium (Cr^{+3}), titanium (Ti^{+2}), and vanadium (V^{+3}) stabilize the HIF-1α by inactivating the PH enzyme [12-16]. This results into the accumulation of intracellular HIF-1α (a biochemical milieu,

[a] Department of Biotechnology & Medical Engineering, National Institute of Technology, Rourkela-769008, Odisha, India.
[b] Department of Chemistry, National Institute of Technology, Rourkela-769008, Odisha, India.
* banerjeei@nitrkl.ac.in; Phone : +91-943-850-7035

† Footnotes relating to the title and/or authors should appear here.
Electronic Supplementary Information (ESI) available: [details of any supplementary information available should be included here]. See DOI: 10.1039/x0xx00000x

analogues to the hypoxic condition) and subsequently increases the production of VEGF. Exploiting the aforesaid strategies, Wu et al. (2012 and 2013) showed that copper and cobalt doped mesoporous bioactive glass scaffolds can effectively induce cellular VEGF production and angiogenesis [17-18].

Nickel is a group 'd' metal. The average quantity of nickel present in healthy individual is about 10 mg (0.1 ppm) [19]. The concentration of nickel present in the serum is approximately 0.2 µg/l in normal population [19]. Earlier nickel was considered harmful to human health, causing skin allergies, asthma, inflammation, lung fibrosis, kidney diseases and cancer [20]. Lately, it was realized that the nickel toxicity is dose-dependent therefore, can be used safely in vivo with certain modifications/precautions. Owing to these facts, nickel based materials like stainless steel (15 % Ni) and a number of shape-memory alloys like Nitinol (50 % Ni) [21-22] have now been used in biomedical implants for clinical application. One interesting property of Nickel (especially of Ni^{+2}) is that like many other 'd' block elements (Cu, Co, Cr, Ti, V), it can also stabilize the HIF-1α, therefore, can induce cellular VEGF secretion by creating intracellular hypoxia mimicking condition [23]. Keeping the aforesaid perspective in mind, we hypothesized that incorporation of Ni^{+2} in an osteogenic biomaterial may convert it to a proangiogenic-osteogenic biomaterial which could be a better option for bone tissue engineering.

Synthetic nano-hydroxyapatite (nHAp) has already been regarded as one of the best biomaterials for bone tissue engineering because of its structural and chemical resemblance with bone apatite and for its osteoconductive properties. In natural bone, nano-sized needle-like hydroxyapatite crystals (HAp) are grown in intimate contact with collagen fibers. One interesting feature of the normal bone apatite is that they are calcium deficient in nature and can efficiently exchange cations (Ca^{+2}) and anions [OH^- and $(PO_4)^{-3}$] with the surroundings. It was realized later that the substitution of such ions play a predominant role in the biochemical aspects of these hard tissues. Therefore, replacement of the calcium and hydroxide ions in the synthetic HAp crystal structure with various metal ions (e.g. Mg^{+2}, Zn^{+2}, Mn^{+2}, Co^{+2}, Y^{+3}) has been done for various applications including bone tissue engineering [24]. In relation to our hypothesis, this manuscript delineates the synthesis, physicochemical characterization and biological performance (osteogenic and angiogenic properties) of Ni^{+2} doped nHAp. Very few reports are available on the synthesis, characterization and application of Ni^{+2} doped HAp [25-26]. However, none of the studies pertains to the exploration of proangiogenic-osteogenic properties of Ni^{+2} doped HAp.

Here, Ni^{+2} doped nHAp samples were synthesized via wet chemical precipitation method. The physico-chemical characterization of the synthesized nHAp was carried out by XRD, FT-IR, FESEM, TEM, Zeta analyser, BET surface analyser and protein absorption profiling. Biological properties including osteogenic and proangiogenic potentials of doped nHAp were assessed in vitro by cell cycle analysis, live-dead assay, MTT assay, immunocytochemistry, ELISA and RT- PCR using human osteoblast cell lines (MG-63).

2. Materials and methods

2.1. Materials:

Calcium nitrate tetrahydrate ($Ca(NO_3)_2.4H_2O$), diammonium hydrogen phosphate ($(NH_4)_2HPO_4$), nickel nitrate hexahydrate ($Ni(NO_3)_2.6H_2O$), cetyltrimethylammonium bromide (CTAB) and ammonia solution (25 %) were purchased from Merck, India. Dulbecco's Modified Eagle Media (DMEM), Dulbecco's Phosphate Buffer Saline (DPBS) solution, Trypsin-EDTA solution, Fetal Bovine Serum, antibiotic-antimycotic solution, and MTT assay kit were purchased from Himedia, India. Human VEGF ELISA kit was purchased from Abcam, UK. mRNA isolation kit (RNeasy Mini) and cDNA synthesis kit (MuLV Reverse Transcriptase Plus Kit) were bought from Qiagen and BioBharti LifeSciences Pvt. Ltd., India, respectively. The MG-63 cell line was procured from NCCS, India.

2.2. Methods:

2.2.1. Synthesis of nano-hydroxyapatite and nickel doped nano-hydroxyapatite:

nHAp and Ni^{+2} doped nHAp were synthesized via wet chemical method [27-28]. In brief, 200 ml of 0.05 M $Ca(NO_3)_2.4H_2O$ was taken in a 500 ml glass beaker and placed in a sonicator bath maintained at 80 °C. The pH of the system was maintained at 10-12 by drop- wise addition of NH_4OH. 200 ml of 0.03 M $(NH_4)_2HPO_4$ solution and CTAB in the ratio 1:1 (w/w) was added drop-wise to the $Ca(NO_3)_2.4H_2O$ solution at a constant rate of 1.5 ml/min from a burette. The slurry was allowed to age for 24 h. The slurry obtained was then washed by centrifuging at 6000 rpm for 10 min to remove the unreacted reactants. The precipitate was then dried at 55 °C for 24 h to get the nHAp powder (control – designated as HAP). Nickel doped nHAp samples were prepared by the same method in which different percentage of ($Ni(NO_3)_2.6H_2O$) (1 %, 5 %, and 10 % w/w) was first added to the $Ca(NO_3)_2.4H_2O$ solution. The molar ratio of Ca/P and (Ca+Ni)/P in all the cases were maintained at 1.67. The dried samples were then ball-milled (Pulverlsette 5 planetary ball mill, Fritsch) for 6 h at 350 rpm. nHAp samples corresponding to 1 %, 5 %, 10 % Ni^{+2} doping were designated as N1-HAP, N5-HAP and N10-HAp, respectively.

2.2.2. Physico-chemical characterization

The phase content of the samples was studied using XRD (Ultima-IV, Rigaku). The scanning was done over a range of 20°-60° 2θ at a scanning rate of 5° 2θ /min. The fraction of the crystalline apatite phase present in the powdered sample was calculated using the formula given below and reported as the degree of crystallinity (X_c).

$$KA = B_{1/2} x (X_c)^{1/3}$$

where, X_c is the degree of crystallinity

$B_{1/2}$ is the full-width at half maximum corresponding to the '002' plane

KA is the constant (KA = 0.24)

Further, the lattice parameters 'a' and 'c' of HAp crystal (hexagonal system) were calculated using the formula given below

$$a = (6/\sqrt{3}) \times d_{(300)}$$

$$c = 2 \times d_{(002)}$$

the above formula were derived from the relationship between crystal plane index and interplannar distance for general hexagonal crystal system which is as follows [29]

$$1/ d_{hkl} = [4 (h^2 + k^2 + hk) /3a^2 + l^2/c^2]^{1/2}$$

where, 'd' is the interplanar distance obtained from XRD data (using Bragg's law). h, k, and l are the miller indices of the crystal.

FT-IR analysis of the samples was done by FT-IR spectrophotometer (IR prestige 21, Shimadzu) using KBr pellet. Scanning was done over the range of 400 cm^{-1} - 4000 cm^{-1} in transmittance mode [30]. Extent of doping was measured by inductively coupled plasma optical emission spectrometry (ICP-OES)

(Perkin Elmer optima 5300 DV) [31]. Sample preparation for ICP-OES was done as per the protocol described by Wadekar et al. (2006) [32].In brief , the samples were digested with mixture of conc. Nitric acid (69 %) and conc. Perchloric acid (70 %) in ratio of 2:1 (% v/v). The concentrated acid digest was heated at 50 °C continuously on a hot plate to remove concentrated acids and the solution was diluted with 1 % Nitric acid. Final volume of the digested samples was made upto 25 ml with distilled water and the pH of the final solution was adjusted to ~ 6-7 for ICP-OES analysis. To study the morphology and particle size, both scanning electron and transmission electron microscopy were done. For scanning electron microscopy, powdered samples were sputter coated with gold and then visualized under FESEM (FEI, Nova NanoSEM) at 3kV [33]. For transmission electron microscopy, a drop of dilute suspension of the powdered samples were placed on 100 µm mesh carbon-coated copper grid and dried overnight under vacuum at room temperature. Samples were then investigated using High Resolution Transmission Electron Microscope (JEM 2100, JOEL) at 200 kV [34]. BET surface area analyser (Autosorb-1, Quantachrome Instruments) was used to determine the surface area, pore size and pore volume of the doped samples. The analysis was done following 5-point fast scan procedure [34]. The zeta potential of the nHAp samples was determined using zeta analyser (Nano ZS, Marvelin). For this analysis, 1 mg of the sample was added in 10 ml of injection water (pH 7.0) and sonicated for 10-15 min to break the agglomeration. Then, the suspension was immediately subjected to zeta analysis [35]. For protein absorption study, 10 mg of nHAp powder was incubated in 1 ml of an aqueous solution of bovine serum albumin (BSA) (1200 µg/ml) at 37 °C for 24 h. After incubation, the solution was centrifuged at 8000 rpm for 10 min and the supernatant was collected. The residual protein concentration in the supernatant was determined using Bradford assay. The adsorption of the proteins by the samples were determined by subtracting the residual protein concentration from the total protein concentration [36].

2.2.3. Biological Characterization

Concentration dependent effect of doped nHAp samples on MG-63 cell viability and proliferation was initially assessed by MTT assay. Cells were maintained in DMEM media supplemented with 10 % FBS and 1 % antibiotic antimycotic solution at 37 °C, 5 % CO_2 and 95 % relative humidity in an incubator. At 80 % confluency, cells were harvested and seeded in a 96-well plate at a concentration of 1.5 x 10^4 cells / well. For the selection of nHap concentration (dose) for the cellular studies, cells were treated with doped nHAp samples at three different concentrations (500 µg/ml, 100 µg/ml & 10 µg/ml). The cell viability was analysed after 24 h and 72 h by using MTT assay kit following the manufacturer's instructions. On the basis of this priliminary assay, 100µg/ml concentration was selected for further studies and cell proliferation was assessed for 5 days following the same protocol mentioned above. The cell viability was further analysed by live-dead assay using flow cytometry. For this study, MG-63 cells were seeded in a 6-well plate at a population of 1 x 10^5 cells / well. Cells were treated with the doped nHAp samples at a concentration of 100 µg/ml and cell viability was analyzed after 24 h, 72 h and 120 h. The cell population was stained with 50 µg/ml PI (propidium iodide) in presence of 100 U/ml RNase and analyzed using flow cytometer (FACS Accuri C6, BD Biosciences) [37]. The variations in the cell cycle among the population in response to nHAp samples were analyzed using flow cytometry. For the analysis, the cells were treated with the samples at a concentration of 100 µg/ml for 24 h. Thereafter, the cells were fixed with 70 % ice-cold ethanol, stained with PI dye and analyzed using flowcytometer (FACS Accuri C6, BD Biosciences) [38]. The formation of bone nodule by MG-63 cells was visualized using scanning electron microscopy. For this, the cells were treated with the samples at a concentration of 100 µg/ml for 72 h. Thereafter, cells were fixed with 4% paraformaldehyde, treated with 2 % osmium tetroxide and serially dehydrated with ethanol (30-100 %). Prior to visualization, the cells were sputter coated with gold and imaging was carried out using FEI, Nova NanoSEM at 3kV [39].

The expression of the differentiation marker Runx2 (Runt-related transcription factor 2) and HIF-1α was analyzed using immunocytochemistry. For the analysis, cells were treated with the samples at a concentration of 100 µg/ml. The primary antibodies used for the analysis were anti-HIF-1α antibody (Mouse, anti-human, 1:200 dilution) and anti-runx2 antibody (rabbit anti-human, 1:200 dilution). Secondary antibodies were anti-Rabbit Alexa Flour 488 and anti-Mouse Alexa Flour 488. Actin cytoskeleton and nuclear staining was done using TRITC- phalloidin and Hoechst dyes. The samples were visualized under the confocal microscope (TCS-SP8, Leica), keeping all the imaging parameters same [40]. The image quantification was carried out using NIH ImageJ software. VEGF expression from the MG63 cells was determined using human VEGF ELISA kit (Abcam 100662) as per the manufacturer's instructions [41]. For the analysis, cells were treated with the samples at a concentration of 100 µg/ml for 48 h and the spent media was used to quantify secreted VEGF. Furthermore, expression of VEGF, runx2, and HIF-1α in MG-63 was also checked by RT-PCR. For this, the cells were treated with the samples at a concentration of 100 µg/ml for 48 h. mRNA isolation and cDNA synthesis was carried out using Qiagen RNeasy Mini Kit and BioBharti MuLV Reverse Transcriptase plus Kit, respectively, following the manufacturer's instructions. Further, the gene specific amplification was done using PCR and expression profile was assessed by comparing band intensity. GAPDH was used as a control for the analysis. For the amplification, the primers used include 5' GCACCCATGGCAGAAGGAG 3' (VEGF_F), 5' ACACAGGATGGCTTGAAGATGT 3' (VEGF_R), 5' GTTTACTAAAGGACAAGTCACC 3' (HIF1_F), 5' TTCTGTTTGTTGAAGGGAG 3' (HIF1_R), 5' TCTGGCCTTCCACTCTCAGT 3' (Runx2_F), 5' GACTGGCGGGGTGTAAGTAA 3' (Runx2_R), 5' CATGAGAAGTATGACAACAGCCT 3' (GAPDH_F) and 5' AGTCCTTCCACGATACCAAAGT 3' (GAPDH_R).

2.2.4. Statistical Analysis:

All the experiments were carried out in triplicate and the data are reported as mean ± SD (Standard deviation). For evaluating statistical significance of the data, one way ANOVA was performed.

3. Results

3.1. Preparation of Ni^{+2} doped nHAp

Many research group has prepared nHAp and doped nHAp using number of methodologies such as hydrothermal synthesis, emulsion method, solid state synthesis, wet chemical method, sol-gel method and biosynthesis [42]. Among the techniques mentioned above, wet chemical method has been adopted widely because of process simplicity and controllability. Here, synthesis of nHAp and Ni^{+2} doped nHAp was done by ammoniacal precipitation method. Cationic surfactant CTAB was used as a capping agent to control the size of the nanoparticle [43]. Three different sets of the Ni^{+2} doped nHAp samples were prepared by varying the doping concentration (Table 1). The yield of nHAp and Ni^{+2} doped nHAp was between 0.95 to 1.0 g in all the cases. There was no significant variation in the yield with an increase in the doping percentage. For all the cases,

percentage yield (w/w) was approximately 30 %. In order to gain powder nHAp, the agglomerate was ball-milled after drying. Physical inspection of the powdered nHAp revealed that all the samples were free-flowing. Pure nHAp was milky white in colour, while Ni^{+2} doped nHAp were whitish green (Fig.S1. Supplementary Section).

Table 1. Composition, yield and physical appearance of nHAp and Ni^{+2} doped nHAp

S.No	Samples	Composition	$[Ca(NO_3)_2.4H_2O + Ni(NO_3)_2.6H_2O]$ g/200ml	$[(NH_4)_2HPO_4]$ g/200ml	Yield (g)	Colour
1.	HAP	Hydroxyapatite [Ca/P: 1.67]	2.36 + 0.0	0.79	1.00±0.03	Milk White
2.	N1-HAP	Hydroxyapatite + 1%(w/w)Nickel [(Ca+Ni)/P: 1.67]	2.36 + 0.0236	0.796	0.97±0.01	Creamy White
3.	N5-HAP	Hydroxyapatite + 5%(w/w)Nickel [(Ca+Ni)/P: 1.67]	2.36 + 0.118	0.822	0.99±0.09	Greenish White
4.	N10-HAP	Hydroxyapatite + 10%(w/w)Nickel [(Ca+Ni)/P: 1.67]	2.36 + 0.236	0.854	1.00±0.01	Greenish White

3.2. Physico-chemical characterization:

3.2.1. Morphological analysis:

Biological performance of nHAp depends immensely on the size and the shape of the particles. Here, the morphology of the nHAp and the Ni^{+2} doped nHAps was primarily investigated using FESEM. It was evident from the micrographs (Fig. 1A) that all the samples formed globular agglomerate while the individual particles had a size ranging between 15-25 nm. The agglomerates appeared more compact in case of N10-HAP. No significant heterogeneity in the size and the shape was observed among the samples. TEM micrograph showed that all the Ni^{+2} doped nHAp samples had an elongated spheroid shape. Image analysis of the TEM micrograph further confirmed that the size of all the samples were in the nano-range with an average ferret diameter lied in the range of 15–17 nm (Fig. 1B and 1C). The average ferret diameter for HAP was 17.2 ± 3.9 nm, while the same for N1-HAP, N5-HAP and N10-HAP was 15.6 ± 3.3, 16.8 ± 3.0 and 15.1 ± 3.0 nm, respectively. The variation in the particle size among the samples was insignificant ($p>0.05$), except for N10-HAP whose particle size was significantly less than nHAp ($p <0.05$). Consistent with the FESEM, TEM results also demonstrated a greater particle agglomeration in N10-HAP samples in comparison to other samples. TEM diffraction pattern (Inset Fig. 1B) revealed that all the samples were partially crystalline with the fringes composing of both bright dots and diffused lines. The calculation of 'd' spacing for 002 plane ('d_{002}') showed gradual decrease with an increase in Ni^{+2} doping concentration. The value of 'd_{002}' spacing was similar for samples nHAp and N1-HAP with value of 0.3644 nm and 0.3642 nm respectively. However, the same for samples N5-HAP and N10-HAP decreased to 0.3624 nm and 0.3578 nm, respectively (Table 2).

3.2.2. Analysis of extent Ni^{+2} doping

Quantification of Ni^{+2} doping is essential for understanding of the composition-activity relationship of doped nHAp. In the present study, the presence of dopant and extent of doping was confirmed by ICP-OES analysis. The result showed that ammoniacal precipitation method could successfully be used for the preparation of Ni^{+2} doped nHAp. A gradual increase in the percentage of doping was observed with an increase of Ni^{+2} concentration. However, the actual doping was found to be less than the theoretical value (Fig. 1D). The actual percentage of Ni^{+2} doping was found to be 0.26, 0.87, and 2.97 % (w/w) for samples N1-HAP, N5-HAP and N10-HAP, respectively. Analysis showed that in all the cases, actual doping was less than 30 % of the theoretical value. It is important to mention that the extent of doping were statistically significant for all the samples ($p < 0.05$).

RSC Advances

PAPER

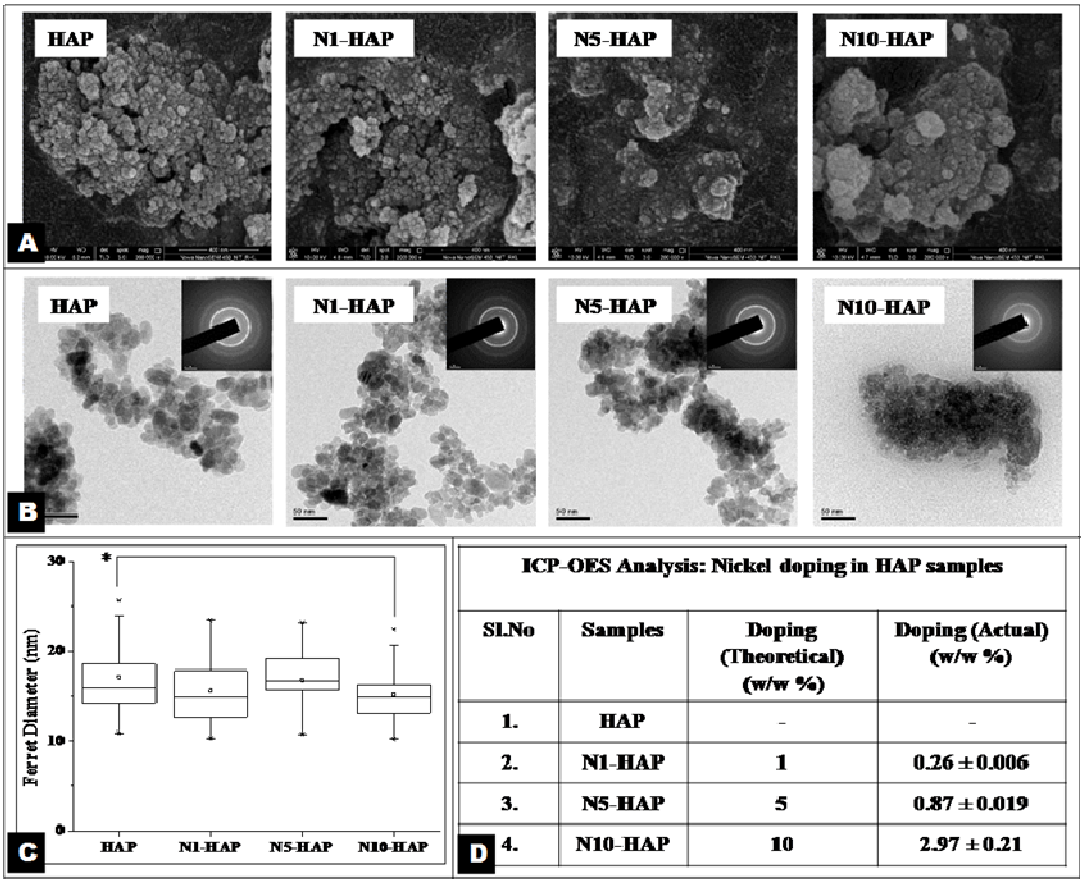

ICP-OES Analysis: Nickel doping in HAP samples

Sl.No	Samples	Doping (Theoretical) (w/w %)	Doping (Actual) (w/w %)
1.	HAP	-	-
2.	N1-HAP	1	0.26 ± 0.006
3.	N5-HAP	5	0.87 ± 0.019
4.	N10-HAP	10	2.97 ± 0.21

Fig. 1. [A] FESEM micrographs of nHAp and Ni^{+2} doped nHAp. [B] TEM Images of nHAp and Ni^{+2} doped nHAp. [C] Nano particle size distribution. TEM Image based analysis was done using NIH-ImageJ software. For each analysis 25 individual particles were considered ($p< 0.05$). [D] ICP-OES analysis of percentage of Ni^{+2} doping with respect to calcium content (w/w). Results were expressed as Mean ± S.D of three independent experiments ($p <0.05$).

3.2.3. XRD Analysis

XRD is a useful tool for confirming the apatite phase. This characterization is essential because little variation in the process parameters often results in significant changes in the composition (phase), crystal structure and percentage crystallinity of a material which altogether have a profound effect on the performance of the material. Analysis of the XRD profiles of the doped nHAp did not show any additional peaks corresponding to that of nickel (Fig. 2A). The characteristic peaks of HAp at 32°, 33° and 34° 2θ, corresponding to the planes (211), (300) and (202), respectively, were found in all the samples. Analysis of the crystal structure showed that the magnitude of the lattice parameter 'c' was same for HAP, N1-HAP, N5-HAP and N10-HAP. It is important to mention that sample N5-HAP was the most crystalline (64 %) in nature while N10-HAP had the least crystallinity (22 %). The same for HAP and N1-HAP was found around 42 % (Table 2).

3.2.4. Molecular characterization by FT-IR:

FT-IR analysis, in conjugation with XRD, is often used to confirm the molecular identity of HAp. Here, the FTIR analysis of the samples revealed the characteristic peaks of HAp (Fig. 2B) [44]. The peaks at 630 cm^{-1}, 600 cm^{-1} and 550 cm^{-1} corresponding to free OH and υ_4 vibrational state of the phosphate group $(PO_4)^{-3}$, respectively, appears less prominent with the increase in the nickel doping and becomes merged in case of N10-HAP, where the doping was highest. All the samples showed a common peak of H-bonded OH stretching at 3570 cm^{-1}. However, in case of N5-HAP and N10-HAP, a new peak appeared at 3640 cm^{-1} which corresponds to free OH^- stretching. The bands at 1470 cm^{-1} and 870 cm^{-1} corresponding to $(CO_3)^{-2}$ were observed due to the atmospheric CO_2 adsorption. Adsorbed water gave two kinds of band, O-H bending (1640 cm^{-1}) and O-H stretching (3450 cm^{-1}). The peak at 1640 cm^{-1} became wider in N10-HAP and N1-HAP, which may be due to the crystal deformation.

RSC Advances

PAPER

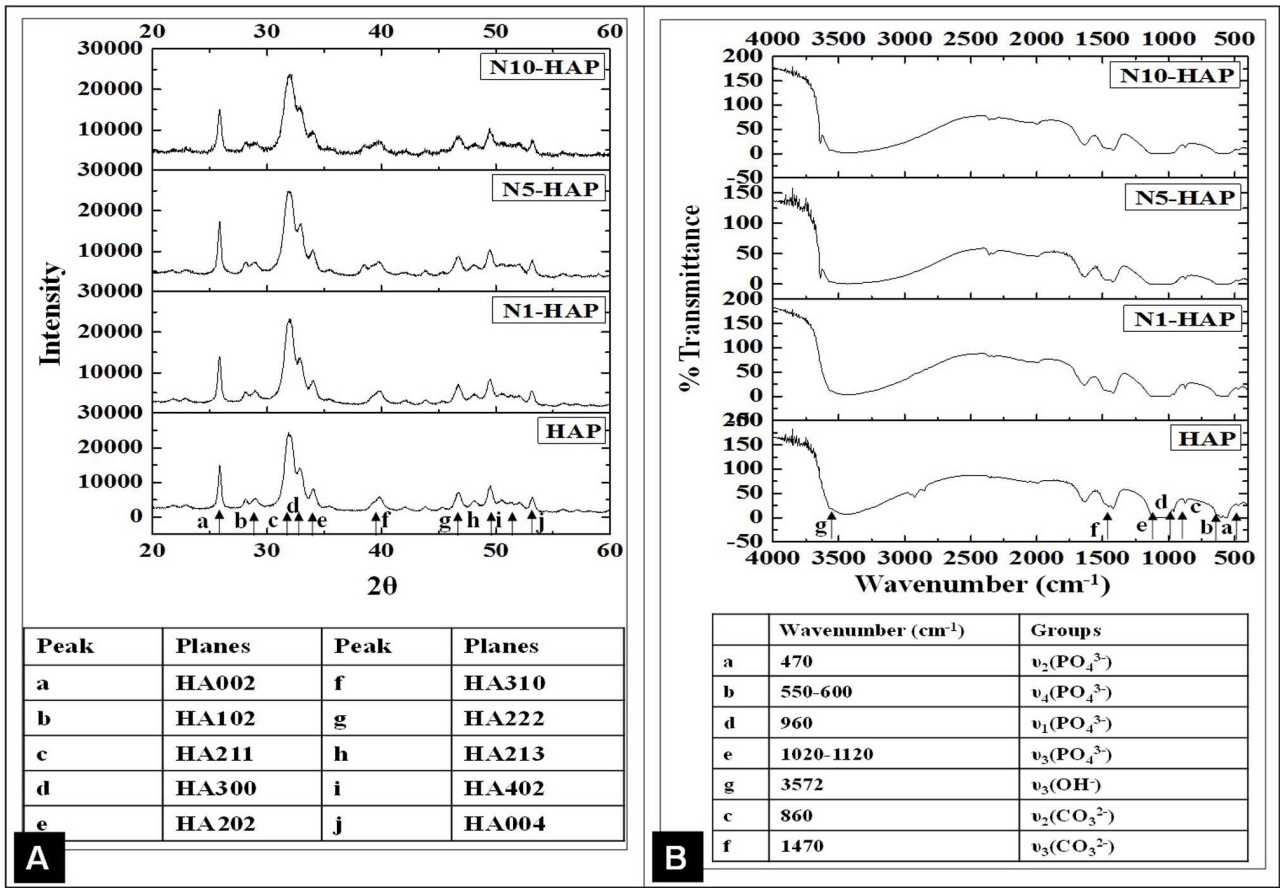

A

Peak	Planes	Peak	Planes
a	HA002	f	HA310
b	HA102	g	HA222
c	HA211	h	HA213
d	HA300	i	HA402
e	HA202	j	HA004

B

	Wavenumber (cm^{-1})	Groups
a	470	$\upsilon_2(PO_4^{3-})$
b	550-600	$\upsilon_4(PO_4^{3-})$
d	960	$\upsilon_1(PO_4^{3-})$
e	1020-1120	$\upsilon_3(PO_4^{3-})$
g	3572	$\upsilon_3(OH^-)$
c	860	$\upsilon_2(CO_3^{2-})$
f	1470	$\upsilon_3(CO_3^{2-})$

Fig. 2. [A] XRD analysis of nHAp and Ni^{+2} doped nHAp. Important characteristic peaks are marked in the figure, and its corresponding crystal planes were mentioned in the embedded table. [B] FT-IR analysis of nHAp and Ni^{+2} doped nHAp. Important characteristic peaks are marked in the figure, and its corresponding bond perturbation were mentioned in the embedded table.

Table 2. Crystal parameters of nHAp and Ni^{+2} doped nHAp. Percentage crystallinity and 'd' spacing were calculated using the XRD and TEM diffraction data corresponding to 002 plane. For the analysis of crystal lattice parameters, 'a' and 'c', 300 and 002 planes were considered.

S.No	Samples	% Crystallinity	Crystal lattice parameters (Å)		'd'-spacing (nm)
			'a'	'c'	
1.	HAP	42.0	9.37	6.88	0.3644
2.	N1-HAP	42.0	9.43	6.90	0.3642
3.	N5-HAP	64.0	9.37	6.88	0.3624
4.	N10-HAP	22.0	9.43	6.90	0.3578

3.2.5. Analysis of the surface area of the nHAp by BET:

The surface area of the nanoparticles was determined by nitrogen absorption analysis (BET) using a Quantachrome surface area analyser (Table 3). The surface area of HAP was found to be 109.1 m^2/g, in accordance with the values previously reported [34]. The same for N1-HAP, N5-HAP and N10-HAP were 107.6 m^2/g, 111.7 m^2/g and 83.2 m^2/g, respectively. The pore volume was maximum for N5-HAP (0.046 cc/g) and minimum for N10-HAP (0.034 cc/g). HAP and N1-HAP had similar pore volume, around 0.04 cc/g.

3.2.6. Zeta potential of nHAp particles:

Zeta potential of HAP sample was found to be -3.54 mV in pure water (pH 7.0) in accordance with the former reports [45]. It was observed that with Ni^{+2} doping, the zeta potential tends towards more positive. However, the increase in zeta potential was not proportional to the percent nickel doping (Table 3). The highest positive zeta (+3.20 mV, change in 7 unit) was observed for N5-HAP followed by N10-HAP (+1.11 mV, change in 5 unit) and N1-HAP (-1.04 mV, change in 3 unit), respectively.

3.2.7. Protein adsorption by the nHAp particles:

Absorption of bovine serum albumin (BSA) by the synthesized nHAp particles was tested at physiological condition (37 °C, pH 7.4) for 24 h. Pure nHAp and Ni^{+2} doped nHAp samples showed a similar protein adsorption. The average protein adsorbed was around 900

µg/10mg of the HAp samples. Analysis showed there was no significant variation ($p > 0.05$) in the extent of the protein absorption among the four samples (Table 3).

Table 3. Analysis of surface area, pore volume, zeta potential and protein absorption. The data were mean of three independent experiments and presented as Mean ± S.D.

S.No	Samples	Surface area (m^2/g)	Pore volume (cc/g)	Zeta potential (mV)	Protein adsorption (µg)
1.	HAP	109.1	0.041	-3.5	881±19.5
2.	N1-HAP	107.6	0.040	-1.0	885±7.4
3.	N5-HAP	111.7	0.046	3.2	873±18.4
4.	N10-HAP	83.2	0.034	1.1	878.5±1.2

3.3. Biological characterization:

3.3.1. Study of cell proliferation by MTT assay

The MTT assay was performed to check the effect of nHAp and doped nHAp on cell viability and proliferation of MG-63 cells (Fig. 3A & 3B). Initially, the cells were treated with different doses of nHAp and doped nHAp for 3 days and cell viability was measured (Fig.3A). At day 1, it was observed that the cell viability corresponding to all three doses were comparable/higher than control (cells cultured on tissue culture plate without any treatment). For HAP and N10-HAP, the maximum viability was observed for 100 µg/ml concentration followed by 10 µg/ml. In case of N1-HAP and N5-HAP, cell viability was highest for 500 µg/ml concentration. N5-HAP and N10-HAP treated cells showed a concentration dependent decrease in the proliferation (500 µg/ml < 100 µg/ml < 10 µg/ml) on day 3. Interestingly, for the dose of 500 µg/ml, the cell viability was found even less than control in case of N5-HAP and N10-HAP treated cells. A critical analysis of these data revealed that for all the groups, a dose of 100 µg/ml of samples ensures cell viability and proliferation comparable to the control at day 1 and day 3. Therefore 100 µg/ml sample concentration was chosen as preferred dose for rest of the study. A review of literature further confirmed that 100-200 µg/ml of nHAp can be used in vitro for biological study [46].

Effect of doped samples (at a concentration of 100 µg/ml) on long term cell proliferation was further checked by MTT assay (Fig. 3B). HAP showed the highest cell proliferation in comparison to all other samples upto day 5. On day 1, there was no significant variation in the cell proliferation among all the groups ($p > 0.005$). On day 3, HAP treated cells showed significant proliferation with respect to Ni^{+2} doped nHAp treated groups ($p < 0.005$). However, no significant variation in the cell proliferation was observed among N1-HAP, N5-HAP, and N10-HAP. On day 5, significant variation in cell proliferation was observed among all the groups ($p<0.005$) where N10-HAP treated cells showed least proliferation. Comparative analysis of the proliferation rate showed that HAP treated cells maintained a consistent growth rate (1.31 fold and 1.33 fold increase in OD value from day 1 to day 3 and day 3 to day 5) which was found highest for all the samples. For all the Ni^{+2} doped nHAp samples, cell growth from day 1 to day 3 was almost same (1.27 to 1.32 fold increase). But from day 3 to day 5, it was observed that the growth rate was retarded with the increase in the Ni^{+2} doping percentage in case of N5-HAP (0.94 fold) and N10-HAP (0.67 fold).

3.3.2. Study of cell viability by Live-Dead Assay:

Long-term post-treatment cell viability of MG-63 cells was further confirmed by flow cytometry based live-dead assay. The study showed that there was no significant cell death for any treatment group irrespective of the rate of cell proliferation. Percentage of live cells in the total cell population for all the treatment groups were more than 90 % (Table 4). A statistical analysis showed that there was no variation in cell viability among all the groups ($p>0.1$). This suggested that all the Ni^{+2} doped nHAp were highly cytocompatible.

Table 4. Analysis of the percentage of live cells after sample treatment at a concentration of 100 µg/ml. The assay was performed by flow cytometry using PI. Data were expressed as Mean ± S.D (n=3).

Live Dead Assay: Percentage of live cells					
	Control	**HAP**	**N1-HAP**	**N5-HAP**	**N10-HAP**
Day1	94.9±1.2	94.9±1..0	93.4±1.5	92.7±1.5	89.9±2.5
Day3	94.2±0.9	91.7±0.5	93.3±1.1	92.9±0.07	94.5±1.1
Day5	95.1±1.8	92.1±1.5	92.1±1.1	91.1±0.9	92.3±0.1

3.3.3. Cell cycle analysis

Cell cycle analysis (Fig. 4) showed that nickel doping did not perturb normal cell cycle progression. For all the treatment groups, distribution of cell populations in different phases was similar to that of control (tissue culture plate) indicating the absence of any prominent effect of nickel doping on the cell cycle (Fig.4A). For all the treatment groups, major fraction of the cell population lied in the G0/G1 phase of the cell cycle (~ 51-60 %) with sample N5- HAP showing highest fraction (approx. 60 %). More interestingly, N5-HAP had least fraction of the cell population in S phase (10.77 %). On the other hand, least fraction in G2/M phase was observed in N10-HAP treated group (Fig. 4B).

RSC Advances

PAPER

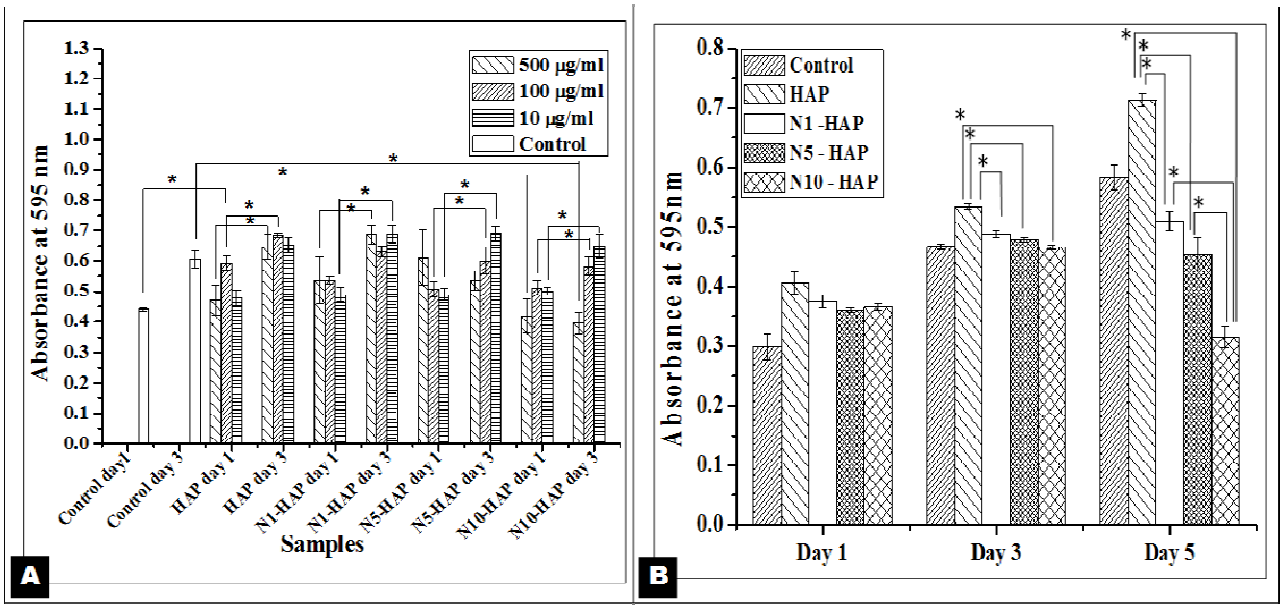

Fig. 3. Cell viability and cell proliferation study by MTT assay. [A] Cells were treated with Ni^{+2} doped nHAp at concentrations of 500µg/ml, 100 µg/ml and 10 µg/ml. Data were expressed as Mean ± S.D (n=3). Statistical significance was checked for p< 0.05. [B] Cells were treated with Ni^{+2} doped nHAp samples at a concentration of 100 µg/ml for the respective days (1, 3 & 5). Data were expressed as Mean ± S.D (n=3). Statistical significance was checked for p< 0.005.

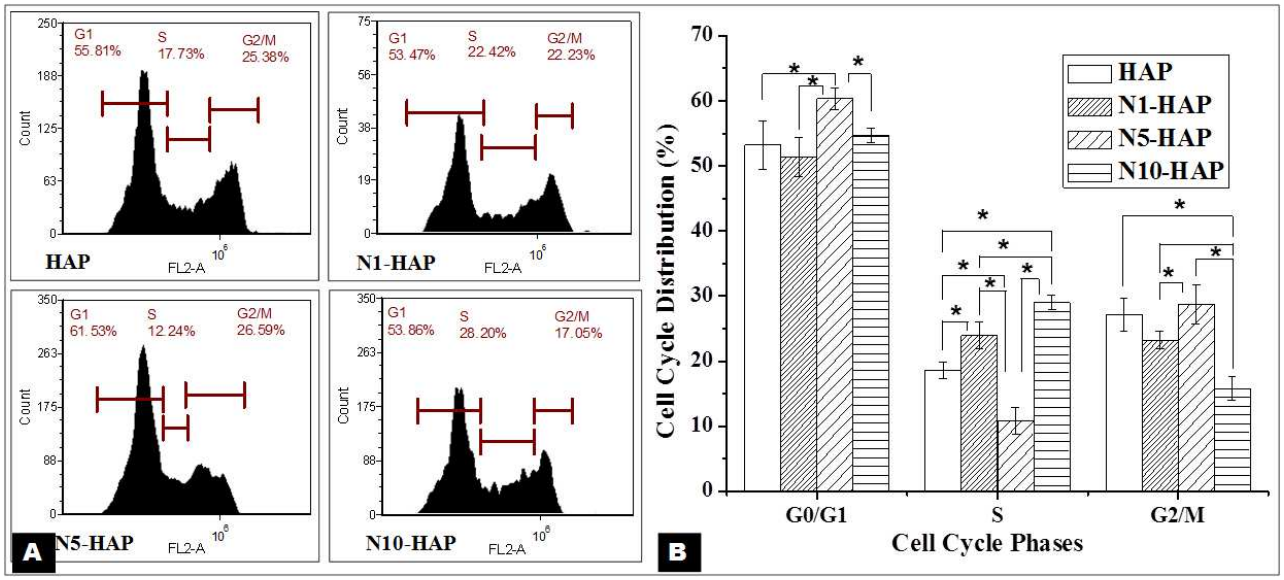

Fig. 4. Study of the cell cycle after 24 h of treatment. Cells were treated with Ni^{+2} doped nHAp at a concentration of 100 µg/ml for a period of 24 h. Experiments were done in triplicate. [A] Representative cell cycle histograms for each sample were presented. [B] Quantitative analysis of cell cycle data. Data were expressed as Mean ± S.D (n=3). Statistical significance was checked for p< 0.05.

3.3.4. Differentiation of osteoblasts

SEM micrographs (Fig. 5A) taken after 3 days of the sample treatment, showed a clear evidence of bone matrix deposition and nodules formation in case of all the samples. All the adherent bone cells appeared healthy and embedded in the bone matrix. Among the four treatment groups, N5-HAP and N10-HAP induced multiple nodule formations supporting their better osteogenic potentials. Furthermore, the confocal images demonstrated little but a significant increase in Runx2 expression (1.3 fold) in case of N10-HAP treated group in comparison to HAP (p <0.005). However, the

variation was found insignificant among HAP, N1-HAP, and N5-HAP treated groups. The increase in the Runx2 expression for N10-HAP was also found statistically significant with respect to N1-HAP and N5-HAP treated groups. A qualitative analysis of immunocytochemistry micrograph showed the localization of Runx2 throughout the cell rather than the nucleus (Fig. 5B, Fig. 5C). It is important to mention that the RT-PCR analysis did not show any sample specific variation in the Runx2 expression among the four groups (Fig. 5D). This clearly suggests that the presence of nickel did not affect the expression of Runx2 significantly, and consequently the differentiation of the MG-63 osteoblast cells.

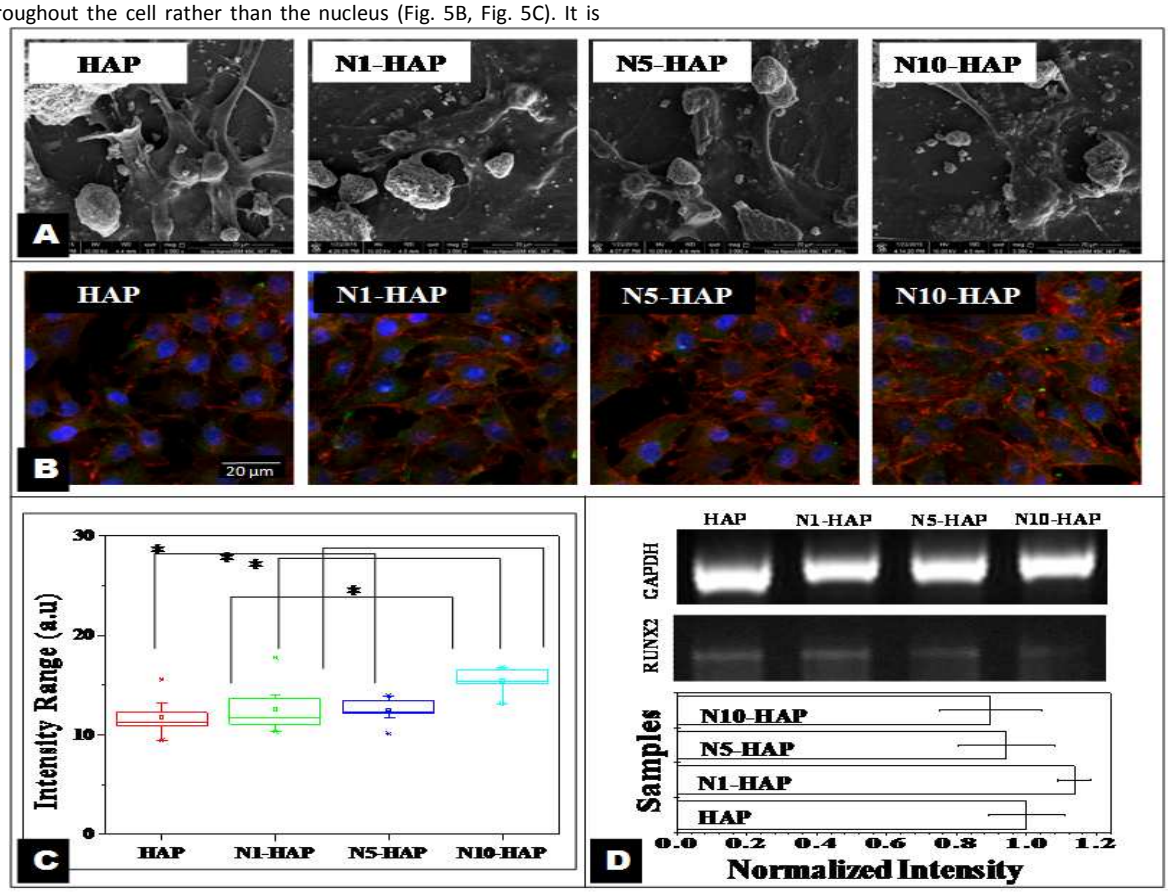

Fig. 5. [A] SEM images of cells cultured in presence of nHAp and Ni^{+2}doped nHAp (at a concentration of 100 µg/ml) at day 3. [B] Confocal micrographs of cells cultured in presence of nHAp and Ni^{+2}doped nHAp (at a concentration of 100 µg/ml) at day 3. Red [F actin], Blue [DAPI] and Green [Runx2]. [C] Quantitative image analysis of Runx2 expression. Intensity was calculated for 10 cells. Statistical significance was checked for p< 0.005. [D] Study of Runx2 expression by RT-PCR. Data were expressed as Mean ± S.D (n=3). Statistical significance was checked for p< 0.05.

3.3.5. Expression of VEGF

The expression of VEGF was measured by ELISA (Fig. 6A). The results showed 2.3 fold, 3.5 fold and 3.8 fold increase in the VEGF expression for samples N1-HAP, N5-HAP and N10-HAP, respectively, in comparison to HAP after 48 h of treatment. The increase in the extracellular VEGF expression was found statistically significant ($p<0.005$) for any two treatment groups including control. In consistency with the ELISA results, RT-PCR based analysis further confirmed an increase in VEGF gene expression at mRNA level with an increase in Ni^{+2} doping concentration. An image-based analysis of the PCR band intensity (amplicons) showed that the maximum VEGF expression was obtained for N10-HAP (2 fold), followed by N5-HAP (1.7 fold) and N1-HAP (1.5 fold), respectively, in comparison to HAP (Fig. 6B).

3.3.6. Expression of HIF-1α

Confocal micrographs of the immuno-stained cells showed an increase in the HIF-1α expression with Ni^{+2} doping. HIF-1α was found spatially distributed around the nucleus (Fig. 6C). Image analysis further revealed that the average expression of HIF-1α was highest in case of N5-HAP (3.3 fold), followed by N10-HAP (1.6 fold), N1-HAP (1.1 fold) and HAP, respectively. The increase in the HIF-1α expression for sample N5-HAP was statistically significant with respect to other three groups ($p<0.05$). Interestingly, the difference in HIF-1α expression between HAP and N1-HAP was not statistically significant (Fig. 6D). RT-PCR analysis showed that there was a minor variation in the HIF-1α expression at mRNA level. The expression of HIF-1α for all the Ni^{+2}doped nHAp was similar to pure nHAp irrespective of doping concentration. Among the Ni^{+2} doped nHAp samples, N10-HAP showed marginally higher expression. However,

the variation was found to be statistically insignificant with respect to other treatment groups (Fig. 6E).

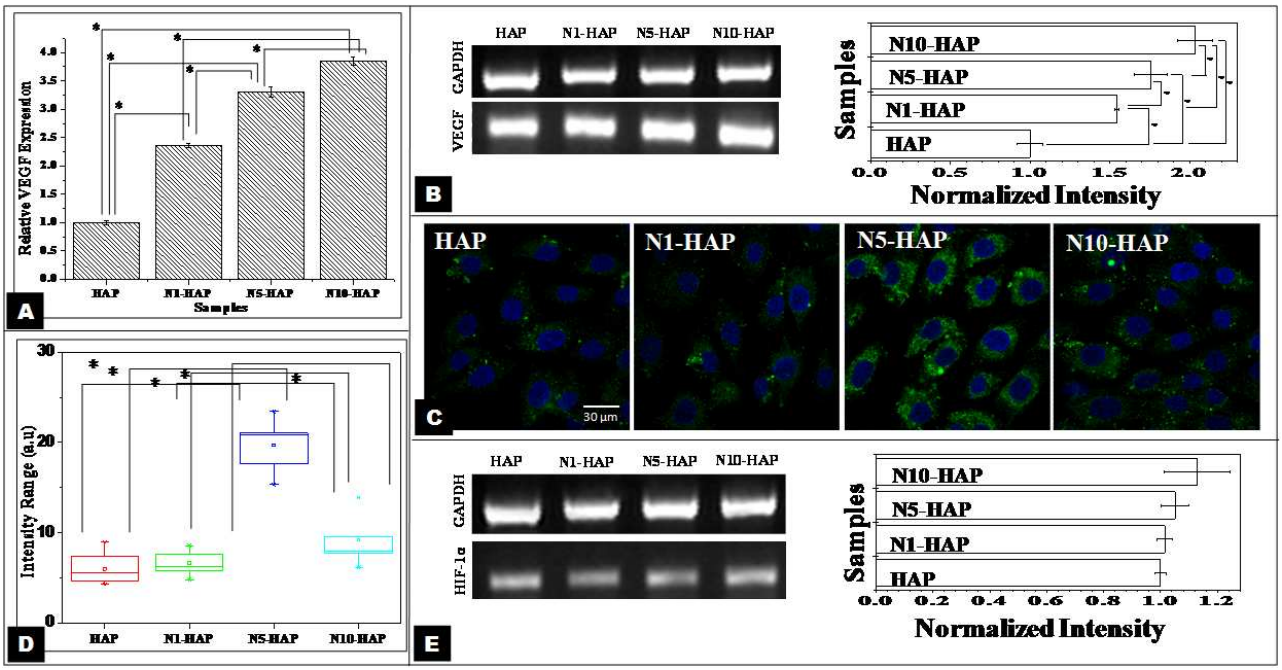

Fig. 6. [A] Analysis of VEGF expression by ELISA. Cells were treated with Ni^{+2} doped nHAp at a concentration of 100 µg/ml for a period of 48 h. Data are expressed as Mean ± S.D. [B] Study of VEGF mRNA expression by RT-PCR. Data were expressed as Mean ± S.D (n=3). Statistical significance was checked for p< 0.05 [C] Study of HIF-1α expression by MG-63 cells after 12 h post treatment with Ni^{+2} doped nHAp (at a concentration of 100 µg/ml) by immuno-cytochemistry. Confocal micrographs of the cells [Red (F actin), Blue (DAPI) and Green (HIF-1α)]. [D] Quantitative image analysis of HIF-1α expression. Intensity was calculated for 10 cells. Statistical significance was checked for p< 0.005. [E] Study of HIF-1α mRNA expression by RT-PCR. Data were expressed as Mean ± S.D (n=3). Statistical significance was checked for p< 0.05.

4. Discussion

So far only few reports are available on Ni^{+2} modified HAp. Neelakandeswari et al. (2012) and Wakamura et al. (1998) reported Ni doped HAp synthesis using coprecipitation-ion exchange and microwave assisted technique [26, 47]. Guerra-Lopez et al. (2000, 2001) previously reported the influence of nickel on calcium HAp crystallization by wet chemical method [48-49]. This is the first report on the synthesis of Ni^{+2} doped nHAp by wet chemical method.

Our study showed that yield of Ni^{+2} doped nHAp was consistent (Table 1) for dopant concentration ranging 1 % w/w to 10 % w/w. The study showed that the intensity of sample colour increased as the percentage of doping was increased and this may be because of the doping or absorption of hexaquanickel (II) ion (formed in the reaction solution) to the HAp. A similar observation was reported and explained by Tank et al. (2013) and Yan Li et al. (2010) when they doped Co^{+2} and Cu^{+2}, respectively in HAp [43, 50].

The extent of doping is associated with the variation in the functional properties of HAp and metal ion toxicity. ICP-OES results clearly revealed that the actual nickel concentration in the doped HAp was much lower than the toxic concentration. A critical analysis of the doped nHAp (Fig. 1D) revealed that the actual nickel doping was less than that of expected theoretical percentage doping. The variation in actual doping was found significant for all the samples ($p < 0.05$). In recent report, Guerra Lopez et al. (2001) demonstrated that the percentage doping in case of transition metals including nickel generally occurs at 1/3rd concentration of the theoretical value [49]. This may probably happen due to the formation of stable amine coordination complex of nickel at the basic pH, maintained for the synthesis of nHAp. These complex ions are bigger and bulky, and thus fail to get incorporated into the HAp crystal lattice [47]. The size and the shape of the nHap crystal are very crucial for bone tissue engineering applications. During in vivo bone remodelling, needle like nHAp is synthesized inside the groves of collagen helices. The size of native nHAp crystals varies between (5 nm - 20 nm) [51]. CTAB, being a cationic surfactant, controls the nucleation and particle size of nHAp by providing an in situ miceller soft template [28]. In the present study, we also used CTAB during the synthesis for the same purpose. The average size (determined by average ferret diameter) of the synthesized nHAp lied in the range of 14 to 18 nm. The size of N10-HAP particles was found significantly smaller than the other samples ($p< 0.05$). However, the synthesized nHAp particles were elongated spheroid in shape and not needle-like (Fig 1A and 1B). Such deviation in particle shape may occur due to the low concentration of CTAB or high pH of the medium. From FESEM and TEM micrographs (Fig. 1A and 1B), it was observed that the N10-HAP nanoparticles formed more agglomerates in comparison to other samples, which may be due to its low crystallinity [52]. The XRD analysis showed that the sample N10–HAP has percentage crystallinity of only 22 % (Table 2), which

could be accounted for its higher agglomeration potential. The doping of metal ion in HAp crystal results in the deformation of the crystal structure. Sallam et al. (2012) reported that chromium doping in the HAp led to alteration in the crystal structure as manifested by broadening of the XRD peaks [53]. In earlier reports, the Ni^{+2} doped HAp synthesised by co-precipitation and ion substitution method showed peak broadening [47, 54]. Interestingly, herein, no such peak broadening was observed, which implies that Ni^{+2} doping did not distort the apatite crystal much. The minimal variations that occur in the crystal parameter could probably be due the smaller ionic radii of Ni^{+2} (0.72 Å) in comparison to Ca^{+2} (0.99 Å). On the contrary, the crystallinity of the nHAp decreased greatly with an increase in the nickel doping (Fig. 2A, Table 2). TEM analysis showed that there was change in the 'd' spacing value corresponding to 002 plane with an increase in the nickel concentration (Table 2) and the difference become approximately 0.01 nm for N10-HAP with respect to HAP.

The FT-IR analysis (Fig. 2B) revealed that with the increase in the doping concentration, the peaks for υ3 stretching (1100 - 1000 cm^{-1}) and υ_2 bending (470 cm^{-1}) of $(PO_4)^{-3}$ became less prominent. These results were found in accordance with Guerra-López et al. (2001) and G. Gergely et al. (2010) [49, 55]. This may be due to the mild variation in the ionic environment of the crystal lattice that leads to an alteration in the stretching field. In addition to the characteristic peaks for the bound water at 1640 and 3450 cm^{-1}, a new peak appeared at 3640 cm^{-1}, attributing to the free OH stretching, which became more intense with the increase in the doping concentration.

The surface area and pore volume play a crucial role in determining the absorption of biomolecules on the implant. The BET study showed an overall variation of 23 % and 35 % in surface area and pore volume, respectively, with Ni^{+2} doping. However, no linear correlation exists between Ni^{+2} doping and the aforesaid parameters (Table 3). Among the samples, the least surface area and pore volume was found in case of N10-HAP, which may be due to low average particle size of N10-HAP, as evident from TEM analysis.

The zeta potential of the nano materials influences its biological performance in a number of ways including protein adsorption, cell-material interaction and cellular uptake. Doping of the metal ions may change native zeta potential of HAp by altering the surface charge density. At physiological pH, the zeta potential of the synthesized nHAp was found to be negative [56] and the metal ion doping results in a variation in its zeta potential. A variation of less than 10 mV was observed with an increase in the nickel concentration from 0 to 10 % w/w. Moreover, the increase was not found directly proportional to the nickel concentration. Such low variation in the zeta potential could be accounted by considering low doping evident from ICP-OES analysis (Fig. 1D). Our BET analysis also revealed that the highest pore volume for N5-HAP, which may explain the minor anomaly in the zeta potential of N5-HAP. The greater pore size may cause higher entrapment of the positive ions in the pore of the particles, thereby, contributing to the excess zeta.

The protein adsorption onto the implant plays a vital role in determining the host immune response towards the implant [57]. Post implantation, a number of plasma proteins including serum albumin, immunoglobins, fibrinogen and fibronectin interact with the biomaterial surface. Hence, BSA was used as a model protein to study the protein adsorbing potential of the Ni^{+2} doped nHAp. The protein adsorption by nHAp depends on its surface area and zeta potential, more specifically on the charge distribution of Ca/Ni and phosphate ions over the crystal surface, involved in the electrostatic interaction with the proteins [58]. Protein absorption result clearly implied that the doping of nickel did not have any influence on the protein adsorption capacity of the nHAps (Table 3). A critical analysis showed that HAP and N1-HAP had similar surface area and zeta properties, owing to same BSA absorption. In addition, protein absorption capacity of N5-HAP was similar to HAP and N1-HAP. However, the zeta potential of N5-HAP was relatively more positive in comparison to others. The nHAp pore diameter and intermolecular repulsion of BSA may provide a clue for such observation. The average pore diameter for all the samples was less than 1 nm (data not shown) which is much lower than the hydrodynamic radius of BSA. Therefore, BSA molecule cannot be accommodated inside these pores. On the other hand, electrostatic repulsion between two adjacent BSA molecules may also prevent the absorption of too many BSA molecules on the nHAp surface.

In the context of bone tissue engineering, biomaterials are generally classified as either osteoconductive or osteoinductive. Synthetic HAp are found to be osteoconductive, supporting the osteoblast viability and proliferation [59]. So far many efforts have been made to improve the osteoconductive property of HAp. Bose et al. (2013) showed an enhanced proliferation of human osteoblast cells in response to treatment with metal ions (Si^{+2}, Sr^{+2}, Mg^{+2} and Zn^{+2}) doped tri-calcium phosphate TCPs [60]. Webster et al. (2010) reported a similar improvement in osteoconductivity of HAp by selective doping of bivalent and trivalent metal ions like Mg^{+2}, Zn^{+2}, La^{+3}, Y^{+3}, In^{+3}, and Bi^{+3} into the HAp [24]. In recent reports, Wu et al. (2012 and 2013) have proven that Cu and Co doped bioglass are highly cytocompatible and support osteoconduction [17-18]. Nickel is also a 'd' block transition metal and Ryhanen et al. (1997) showed that Ni^{+2} is osteoconductive in nature [61]. As mentioned earlier, Ni has also been used extensively in biomedical implants such as Nitinol based stent and dental implants. Our MTT analysis apparently showed that Ni^{+2} doped nHAp samples help in MG-63 cell proliferation (Fig. 3). Further to quantify the variation in the live population of cells, flow cytometry based live-dead assay clearly indicated that Ni^{+2} doped nHAps are cytocompatible (Table 4). Our MTT study showed that there was a decrease in the cell proliferation rate with time. As mentioned earlier, the two possibilities could be either cell death or cell differentiation. It was evident from the live dead assay that there was no significant cell death in the later phase of the culture. On the other hand, cell cycle analysis (Fig. 4) revealed the presence of prolonged G0/G1 phase. In bone physiology, a high population of cells in G0/G1 often indicates their commitment towards differentiation [62]. Therefore, a higher value of G0/G1 in the case of N5-HAP treated group could be because of the differentiation potential of the material. FACS analysis also showed that the percentage cell population in pro-G0/G1 (a phase associated with apoptosis) was negligible for all groups.

Previously, Gough et al. (2004) outlined that the formation of the nodule is a signature of osteoblast differentiation [63]. FESEM images (Fig. 5A) of bone cells showed that Ni^{+2} doped materials (N5-HAP and N10-HAP) were supporting nodule formations. There are some signature proteins that can be only seen during the period of differentiation of preosteoblasts to osteocytes like Runx2, osterix and osteocalacin. Transcription factor runx2 is one of the signature proteins which is a pre-requisite for the osteogenic differentiation of mesenchymal stem cells [64]. In this case, a marginal but significant increase in Runx2 expression was observed in case of N10-HAP (Fig. 5B, 5C). As Runx2 expression can be activated

through calcium dependent Wnt5 signalling pathway, bivalent metal ions (Ni^{+2}) can act as agonist to Ca^{+2} ions and trigger the expression of Runx2 [50]. It is important to mention that MG-63 is a mature osteoblast. Therefore, Runx2 expression always remains in basal level in MG-63 in comparison to its progenitor. Hence, the average expression of Runx2 was almost similar for all the samples.

ELISA analysis (Fig. 6A, 6B) showed that the doped samples induced significantly higher VEGF expression in comparison to pure HAP. From the literature, it is evident that among various angiogenic factors such as PDGF, FGF, bEGF, etc.; VEGF plays a key role in signalling pathways pertaining to endothelial cell migration, survival and angiogenesis [65]. HIF-1α is one of the key regulators of the VEGF expression [66]. The bivalent metal ions stabilize the HIF-1α, which in turn induce the expression of VEGF. Hence, the Ni^{+2} doped nHAp samples showed better expression of VEGF. In the similar studies, Wu et al. (2012 & 2013) showed that bivalent metal ions (cobalt and copper) incorporated mesoporous bioglasses induced higher level of VEGF expression in human bone marrow derived stromal cells. However, comparison of these results showed 3.8 fold increase in VEGF production for 3.22 % nickel doping (the actual Ni doping in N10-HAP) in comparison to undoped ceramics, while the same was 1.2 fold for 5 % cobalt doping in cobalt doped bioglass [17-18]. This clearly suggest that our Ni^{+2} doped nHAp can induce VEGF more effectively with lower concentration, hence reduce the health risk.

In the present study, the immunocytochemistry profile of HIF-1α showed that the nickel doped HAp samples had a significantly higher expression of HIF-1α (Fig.6C, 6D). Wang et al. (2007) and Malda et al. (2007) showed that HIF-1α, a key regulator of the angiogenic genes, expressed during the bone repair. During morphogenesis, vascularization of the bone callus is the key step for bone formation [10, 67]. Bivalent metal ions such as nickel, cobalt, and copper, etc. mimics hypoxia condition by replacing Fe^{+2} ions, the key cofactor of the prolyl hydroxylase enzyme and thereby, inactivating the enzyme and stabilizing HIF-1α. Interestingly, in this study, we observed that expression of HIF-1α did not show any linear correlation with the nickel doping concentration. In case of HIF-1α expression, N5-HAP showed the highest expression followed by N10-HAP, N1-HAP and HAP, respectively. However, in case of VEGF, the increase in the expression was linear with respect to nickel doping concentration. It was also reported for copper and cobalt doped proangiogenic biomaterials, the VEGF expression profile does not always follow the HIF-1α profile. This might be explained on the basis that VEGF expression does not merely depend on the HIF-1α expression level, but also on the mitogen-activated protein (MAP) kinase activity and subsequent phosphorylation mediated activation of HIF-1α. Hence N10-HAP, which might have a sub-optimal HIF-1α expression followed by better MAP kinases activity [68] and phosphorylated activation of HIF-1α, resulted in better VEGF expression. Another reason could be the interplay of Runx2 with HIF-1α which is supposedly stabilizing HIF-1α by competing with the Von Hippel-Lindau Protein (pVHL) [69]. From the Runx2 immunocytochemistry expression profile, N5-HAP showed better expression of Runx2 followed by N10-HAP. Such higher expression of Runx2 in case of N5-HAP may contribute to higher expression of HIF-1α.

All the results pertaining to the characterization of the effect of Ni^{+2} doped nHAp on MG-63 cells indicate that Ni^{+2} doped nHAp can be used as a VEGF inducing osteoconductive biomaterials for bone tissue engineering. However it is important to mention that although MG-63 is often used as osteoblastic model, but it is actually an osteosarcoma cell line derived from malignant bone tumor. Earlier studies have shown that response of MG-63 towards a biomaterials (interms of proliferation, migration and composition of synthesized ECM) often differed in comparison to that of primary human osteoblast [70-71]. Hence, performance of Ni+2 doped nHAp should also be evaluated using primary human osteoblast cells before preclinical study.

5. Conclusion:

Our study showed that Ni^{+2} doped nHAp particles of narrow size distribution can effectively be prepared by wet chemical precipitation method using CTAB. Doping of Ni^{+2} upto 2.97 % w/w of Ca^{+2} did not cause crystal deformation. Similarly, physical properties like surface area, zeta potential and protein absorption remained almost same with Ni^{+2} doping. All the doped samples were bone cell compatible and osteoconductive. Analysis showed that Ni^{+2} doped nHAp samples were potent inducer of cellular VEGF and the expression of VEGF was directly proportional to the doping concentration of Ni^{+2}. A mechanistic analysis further implied involvement of Ni^{+2} in HIF-1α stabilization followed by increased VEGF expression. Comparison of these results with the relevant literature revealed that the relative VEGF expression per unit quantity of doping was higher in the present case.

In conclusion, Ni^{+2} doped nHAp is a proangiogenic–osteogenic material and could be used in bone tissue engineering. Response of endothelial cells (viability and tube formation) and primary osteoblast against these materials in vitro has to be studied. Moreover, it is important to assess the biological performance of the materials in vivo.

6. Acknowledgement:

1.PSG Institute of Advanced Studies for HR-TEM analysis
2. SAIF, IIT Madras for ICP-OES analysis
3.DBT, Govt of India (RGYI scheme project no. BT/PR6230/GBD/27/391/2012)
4.DBT, Govt of India (RGYI scheme project no. BT/PR6227/GBD/27/390/2012)
5.Prof. T.K.Maiti for providing the molecular biology laboratory facility
6.Centre of Excellence, orthopaedic Tissue engineering and Rehabilitation (TEQIP –II)

7. References

1. M. Frohlich, W. L. Grayson, L. Q. Wan, D. Marolt, M. Drobnic and G. Vunjak-Novakovic, *Current stem cell research & therapy*, 2008, **3**, 254-264.
2. M. Mravic, B. Péault and A. W. James, *BioMed research international*, 2014, **2014**.
3. A. Perets, Y. Baruch, F. Weisbuch, G. Shoshany, G. Neufeld and S. Cohen, *Journal of Biomedical Materials Research Part A*, 2003, **65**, 489-497.
4. M. Sheridan, L. Shea, M. Peters and D. Mooney, *Journal of Controlled Release*, 2000, **64**, 91-102.
5. W. D. Holder Jr, H. E. Gruber, W. D. Roland, A. L. Moore, C. R. Culberson, A. B. Loebsack, K. J. Burg and D. J. Mooney, *Tissue Engineering*, 1997, **3**, 149-160.
6. A. Hasan, A. Paul, N. E. Vrana, X. Zhao, A. Memic, Y.-S. Hwang, M. R. Dokmeci and A. Khademhosseini, *Biomaterials*, 2014, **35**, 7308-7325.
7. S. Baiguera and D. Ribatti, *Angiogenesis*, 2013, **16**, 1-14.

8. R. C. Fields, A. Solan, K. T. McDonagh, L. E. Niklason and J. H. Lawson, *Tissue engineering*, 2003, **9**, 1281-1287.
9. H. Iwaguro, J.-i. Yamaguchi, C. Kalka, S. Murasawa, H. Masuda, S.-i. Hayashi, M. Silver, T. Li, J. M. Isner and T. Asahara, *Circulation*, 2002, **105**, 732-738.
10. Y. Wang, C. Wan, L. Deng, X. Liu, X. Cao, S. R. Gilbert, M. L. Bouxsein, M.-C. Faugere, R. E. Guldberg and L. C. Gerstenfeld, *Journal of Clinical Investigation*, 2007, **117**, 1616.
11. Y.-S. Chun, M.-S. Kim and J.-W. Park, *Journal of Korean medical science*, 2002, **17**, 581.
12. G. Chachami, G. Simos, A. Hatziefthimiou, S. Bonanou, P.-A. Molyvdas and E. Paraskeva, *American journal of respiratory cell and molecular biology*, 2004, **31**, 544-551.
13. W. Feng, F. Ye, W. Xue, Z. Zhou and Y. J. Kang, *Molecular pharmacology*, 2009, **75**, 174-182.
14. K. Vandamme, X. Holy, M. Bensidhoum, D. Logeart-Avramoglou, I. Naert, J. Duyck and H. Petite, *Tissue Engineering Part C: Methods*, 2010, **17**, 311-318.
15. J.-T. Hwang, M. Lee, S.-N. Jung, H.-J. Lee, I. Kang, S.-S. Kim and J. Ha, *Carcinogenesis*, 2004, **25**, 2497-2507.
16. M. Kaczmarek, O. A. Timofeeva, A. Karaczyn, A. Malyguine, K. S. Kasprzak and K. Salnikow, *Free Radical Biology and Medicine*, 2007, **42**, 1246-1257.
17. C. Wu, Y. Zhou, W. Fan, P. Han, J. Chang, J. Yuen, M. Zhang and Y. Xiao, *Biomaterials*, 2012, **33**, 2076-2085.
18. C. Wu, Y. Zhou, M. Xu, P. Han, L. Chen, J. Chang and Y. Xiao, *Biomaterials*, 2013, **34**, 422-433.
19. K. Das, S. Das and S. Dhundasi, *Indian Journal of Medical Research*, 2008, **128**, 412.
20. K. Salnikow, W. G. An, G. Melillo, M. V. Blagosklonny and M. Costa, *Carcinogenesis*, 1999, **20**, 1819-1823.
21. S. Civjan, E. F. Huget and L. B. DeSimon, *Journal of dental research*, 1975, **54**, 89-96.
22. M. Fini, N. N. Aldini, P. Torricelli, G. Giavaresi, V. Borsari, H. Lenger, J. Bernauer, R. Giardino, R. Chiesa and A. Cigada, *Biomaterials*, 2003, **24**, 4929-4939.
23. A. A. Nemec and A. Barchowsky, *The FASEB Journal*, 2008, **22**, 764.763.
24. T. J. Webster, E. A. Massa-Schlueter, J. L. Smith and E. B. Slamovich, *Biomaterials*, 2004, **25**, 2111-2121.
25. H. Lukman, Z. Yaakob, I. Manal and W. R. Wan Daud, *Key Engineering Materials*, 2010, **447**, 770-774.
26. N. Neelakandeswari, G. Sangami, P. Emayavaramban, R. Karvembu, N. Dharmaraj and H. Y. Kim, *Tetrahedron Letters*, 2012, **53**, 2980-2984.
27. N. Monmaturapoj, *Journal of Metals, Materials and Minerals*, 2008, **18**, 15-20.
28. M. Salarian, M. Solati-Hashjin, S. S. Shafiei, A. Goudarzi, R. Salarian and A. Nemati, *Materials Science-Poland*, 2009, **27**.
29. T. Liu, Y. Yan and S. Li, *Journal of Wuhan University of Technology-Mater. Sci. Ed.*, 2008, **23**, 395-398.
30. K. Sanosh, M.-C. Chu, A. Balakrishnan, T. Kim and S.-J. Cho, *Bulletin of Materials Science*, 2009, **32**, 465-470.
31. S. Tay, A. Haseeb, M. R. Johan, P. Munroe and M. Quadir, *Intermetallics*, 2013, **33**, 8-15.
32. M. Wadekar, C. Rode, Y. Bendale, K. Patil, A. Gaikwad and A. Prabhune, *Journal of pharmaceutical and biomedical analysis*, 2006, **41**, 1473-1478.
33. M. Saeri, A. Afshar, M. Ghorbani, N. Ehsani and C. Sorrell, *Materials Letters*, 2003, **57**, 4064-4069.
34. N. Puvvada, P. K. Panigrahi and A. Pathak, *Nanoscale*, 2010, **2**, 2631-2638.
35. L. Chen, J. M. Mccrate, J. C. Lee and H. Li, *Nanotechnology*, 2011, **22**, 105708.
36. D. T. H. Wassell, R. C. Hall and G. Embery, *Biomaterials*, 1995, **16**, 697-702.
37. S. Panseri, C. Cunha, T. D'Alessandro, M. Sandri, G. Giavaresi, M. Marcacci, C. T. Hung and A. Tampieri, *J Nanobiotechnology*, 2012, **10**, 32.
38. K. Cheng, W. Weng, H. Wang and S. Zhang, *Biomaterials*, 2005, **26**, 6288-6295.
39. Z. Shi, X. Huang, Y. Cai, R. Tang and D. Yang, *Acta biomaterialia*, 2009, **5**, 338-345.
40. I. R. Zerbo, A. L. Bronckers, G. De Lange and E. H. Burger, *Biomaterials*, 2005, **26**, 1445-1451.
41. D. Armstrong, A. J. Augustin, R. Spengler, A. Al-Jada, T. Nickola, F. Grus and F. Koch, *Ophthalmologica. Journal international d'ophtalmologie. International journal of ophthalmology. Zeitschrift fur Augenheilkunde*, 1997, **212**, 410-414.
42. M. Sadat-Shojai, M.-T. Khorasani, E. Dinpanah-Khoshdargi and A. Jamshidi, *Acta biomaterialia*, 2013, **9**, 7591-7621.
43. K. P. Tank, K. S. Chudasama, V. S. Thaker and M. J. Joshi, *Journal of nanoparticle research*, 2013, **15**, 1-11.
44. Y. Han, X. Wang and S. Li, *Journal of Nanoparticle Research*, 2009, **11**, 1235-1240.
45. Z. Yan-Zhong, H. Yan-Yan, Z. Jun, Z. Shai-Hong, L. Zhi-You and Z. Ke-Chao, *Nanoscale research letters*, 2011, **6**, 1-8.
46. A. Rajendran, R. C. Barik, D. Natarajan, M. Kiran and D. K. Pattanayak, *Ceramics International*, 2014, **40**, 10831-10838.
47. M. Wakamura, K. Kandori and T. Ishikawa, *Colloids and Surfaces A: Physicochemical and Engineering Aspects*, 1998, **142**, 107-116.
48. J. Guerra-López, R. González, A. Gómez, R. Pomés, G. Punte and C. Della Védova, *Journal of Solid State Chemistry*, 2000, **151**, 163-169.
49. J. Guerra-López, R. Pomes, C. Della Védova, R. Vina and G. Punte, *Journal of Raman Spectroscopy*, 2001, **32**, 255-261.
50. Y. Li, J. Ho and C. P. Ooi, *Materials Science and Engineering: C*, 2010, **30**, 1137-1144.
51. M. Ferraz, F. Monteiro and C. Manuel, *Journal of Applied Biomaterials and Biomechanics*, 2004, **2**, 74-80.
52. Y.-J. Shyong, R.-F. Lin, H.-S. Soung, H.-H. Wei, Y.-S. Hsueh, K.-C. Chang and F.-H. Lin, *Journal of Materials Chemistry B*, 2014.
53. S. M. Sallam, K. M. Tohami, A. M. Sallam, L. I. A. Salem and F. A. Mohamed, 2012.
54. G. Mabilleau, R. Filmon, P. Petrov, M. Baslé, A. Sabokbar and D. Chappard, *Acta biomaterialia*, 2010, **6**, 1555-1560.
55. G. Gergely, F. Wéber, I. Lukács, L. Illés, A. L. Tóth, Z. E. Horváth, J. Mihály and C. Balázsi, *Central European Journal of Chemistry*, 2010, **8**, 375-381.
56. R. L. Williams, M. J. Hadley, P. J. Jiang, N. A. Rowson, P. M. Mendes, J. Z. Rappoport and L. M. Grover, *Journal of Materials Chemistry B*, 2013, **1**, 4370-4378.
57. J. M. Anderson, A. Rodriguez and D. T. Chang, 2008.
58. Z. Zhuang, T. J. Fujimi, M. Nakamura, T. Konishi, H. Yoshimura and M. Aizawa, *Acta biomaterialia*, 2013, **9**, 6732-6740.
59. R. Z. LeGeros, *Clinical orthopaedics and related research*, 2002, **395**, 81-98.
60. S. Bose, G. Fielding, S. Tarafder and A. Bandyopadhyay, *Trends in biotechnology*, 2013, **31**.
61. J. Ryhänen, E. Niemi, W. Serlo, E. Niemelä, P. Sandvik, H. Pernu and T. Salo, *Journal of biomedical materials research*, 1997, **35**, 451-457.

62. M. Carroll, Y. Zhu and A. D. D'Andrea, *Proceedings of the National Academy of Sciences*, 1995, **92**, 2869-2873.
63. J. E. Gough, J. R. Jones and L. L. Hench, *Biomaterials*, 2004, **25**, 2039-2046.
64. T. Komori, *Frontiers in bioscience: a journal and virtual library*, 2007, **13**, 898-903.
65. M. Shibuya, *Cell structure and function*, 2001, **26**, 25-35.
66. D. Shweiki, A. Itin, D. Soffer and E. Keshet, *Nature*, 1992, **359**, 843-845.
67. J. Malda, T. J. Klein and Z. Upton, *Tissue engineering*, 2007, **13**, 2153-2162.
68. Q. Ke and M. Costa, *Molecular pharmacology*, 2006, **70**, 1469-1480.
69. S.-H. Lee, X. Che, J.-H. Jeong, J.-Y. Choi, Y.-J. Lee, Y.-H. Lee, S.-C. Bae and Y.-M. Lee, *Journal of Biological Chemistry*, 2012, **287**, 14760-14771.
70. C. Pautke, M. Schieker, T. Tischer, A. Kolk, P. Neth, W. Mutschler And S. Milz, *Anticancer research*, 2004, **24**, 3743-3748.
71. A. Perez, R. Spears, J. Gutmann and L. Opperman, *International Endodontic Journal*, 2003, **36**, 564-570.